Monthly Notices of the ROYAL ASTRONOMICAL SOCIETY

MNRAS **507,** 3046–3056 (2021) https://doi.org/10.1093/mnras/stab2333
Advance Access publication 2021 August 13

Constraints on warm dark matter from UV luminosity functions of high-z galaxies with Bayesian model comparison

Anton Rudakovskyi,[1,2]★ Andrei Mesinger [3], Denys Savchenko [1,2] and Nicolas Gillet [4]

[1]*Bogolyubov Institute for Theoretical Physics of the NAS of Ukraine, Metrolohichna Str. 14-b, Kyiv 03143, Ukraine*
[2]*Kyiv Academic University, 36 Vernadsky blvd., Kyiv 03142, Ukraine*
[3]*Scuola Normale Superiore, Piazza dei Cavalieri 7, I-56126 Pisa, Italy*
[4]*Observatoire Astronomique de Strasbourg, Université de Strasbourg, CNRS UMR 7550, 11 rue de l'Université, F-67000 Strasbourg, France*

Accepted 2021 August 10. Received 2021 August 10; in original form 2021 June 2

ABSTRACT

The number density of small dark matter (DM) haloes hosting faint high-redshift galaxies is sensitive to the DM free-streaming properties. However, constraining these DM properties is complicated by degeneracies with the uncertain baryonic physics governing star formation. In this work, we use a flexible astrophysical model and a Bayesian inference framework to analyse ultraviolet (UV) luminosity functions (LFs) at $z = 6$–8. We vary the complexity of the astrophysical galaxy model (single versus double power law for the stellar – halo mass relation) as well as the matter power spectrum [cold DM versus thermal relic warm DM (WDM)], comparing their Bayesian evidences. Adopting a conservatively wide prior range for the WDM particle mass, we show that the UV LFs at $z = 6$–8 only weakly favour cold DM over WDM. We find that particle masses of $\lesssim 2$ keV are rejected at a 95 per cent credible level in all models that have a WDM-like power spectrum cutoff. This bound should increase to $\sim$2.5 keV with the *James Webb Space Telescope (JWST)*.

Key words: galaxies: luminosity function – reionization – dark matter.

1 INTRODUCTION

The existence of dark matter (DM) has been proven by an enormous set of astrophysical and cosmological observational data. In the standard cosmological ΛCDM paradigm, DM particles are considered massive, collisionless, and non-relativistic. In this scenario, cosmic structures are formed hierarchically from initial density fluctuations by the merging of smaller objects into larger ones. ΛCDM provides a good description of cosmic microwave background (CMB) and large-scale structure observations.

Nevertheless, some physically motivated extensions of the standard model provide suitable DM candidates with masses in keV range, such as sterile neutrinos (see e.g. reviews in Adhikari et al. 2017; Boyarsky et al. 2019) or gravitinos (Viel et al. 2005). These particles are initially relativistic and subsequently become non-relativistic before the matter-dominated epoch. The matter power spectrum of this so-called warm DM (WDM) is strongly suppressed on scales below the 'free-streaming' length. Thereby, WDM predicts a dearth of small-scale structures compared to cold DM (CDM), potentially alleviating some (putative) tensions between CDM and observations on small scales (see more Klypin et al. 1999; Moore et al. 1999; Bullock & Boylan-Kolchin 2017, but see e.g. Kim, Peter & Hargis 2018). Another motivation for WDM candidates is the tentative detection of the 3.5 keV line in the X-ray spectra of DM-dominated objects (Boyarsky et al. 2014; Bulbul et al. 2014), which may be explained by the decay of 7 keV sterile neutrinos.[1]

If warm DM is in the form of thermal relics (e.g. gravitinos), the matter power spectrum is connected to that of CDM via a transfer function, which depends on the WDM particle mass. As the particle mass increases, the transfer function cut-off scale moves to higher k and predictions in WDM cosmologies become closer to those of CDM. On the other hand, sterile neutrinos do not reach thermal equilibrium with other particles, and their power spectrum also depends on the production mechanism. However, the impact on structure formation is still through an effective suppression of the matter power on small scales.

Constraints on WDM properties generally make use of observations of non-linear small-scale structure, including the Lyman-α forest (Viel et al. 2005, 2013; Baur et al. 2016; Iršič et al. 2017; Baur et al. 2017; Murgia, Iršič & Viel 2018; Garzilli et al. 2019), Milky Way stellar streams (Banik et al. 2019), Milky Way satellites count (Polisensky & Ricotti 2011; Kennedy et al. 2014; Jethwa, Erkal & Belokurov 2018; Nadler et al. 2021a; Newton et al. 2020; Nadler et al. 2021b), number counts and luminosity functions (LFs) of distant galaxies (Pacucci, Mesinger & Haiman 2013; Schultz et al. 2014; Menci et al. 2016a, b; Corasaniti et al. 2017; Menci et al. 2017), gamma-ray bursts (de Souza et al. 2013), and strong

[1]Although the origin of this excess is questioned (see for example Dessert, Rodd & Safdi 2020), there is still a debate on the accuracy of such analysis (e.g. Boyarsky et al. 2021).

★ E-mail: rudakovskyi@bitp.kiev.ua

gravitational lensing (Birrer, Amara & Refregier 2017; Vegetti et al. 2018; Gilman et al. 2019, 2020; Hsueh et al. 2020); see e.g. Enzi et al. (2021) for a recent review of current constraints. Hierarchical structure formation implies that 'typical' structures are smaller (less massive) at higher redshifts. This makes high-redshift observations particularly appealing in constraining WDM.

Unfortunately, in all cases, degeneracy with astrophysics makes robust WDM constraints very challenging (though see the model-independent limits introduced in Pacucci et al. 2013). For example, the Lyman-α flux power spectrum depends on both the DM particle mass as well as the unknown thermal history of the intergalactic medium (IGM). Similarly, galaxy LFs depend on both the abundance of DM haloes as well as the unknown star formation processes inside them (e.g. Dayal, Mesinger & Pacucci 2015; Corasaniti et al. 2017; Villanueva-Domingo, Gnedin & Mena 2018; Khimey, Bose & Tacchella 2020; Yoshiura et al. 2020; Sabti, Muñoz & Blas 2021).

In this work, we re-visit WDM constraints implied by high-z ultraviolet (UV) LFs, within a Bayesian framework (for a review of Bayesian methods in cosmology see e.g. Trotta 2017). In addition to deriving lower bounds on the WDM particle mass,[2] we also use the Bayesian evidence when performing model comparison in WDM and CDM. The Bayesian evidence naturally penalizes needlessly complicated models. We vary the complexity of both the matter power spectrum parametrization (i.e. DM model) as well as the galaxy formation model, using the Bayes factor to penalize the 'fine-tuning' provided by the addition of unnecessary parameters to the models.

This paper is organized as follows: in Section 2, we describe our astrophysical model of the UV LFs, observational data sets and Bayesian framework. In Section 3, we report the results of the model comparison and WDM particle limits. We compare the obtained limits with those reported in other works in Section 4. Finally, we conclude in Section 5. Throughout this paper, we assume *Planck-16* cosmological parameters: $\Omega_\Lambda = 0.685$, $\Omega_m = 0.315$, $\Omega_b = 0.049$, $h = 0.673$, $n_s = 0.965$, and $\sigma_8 = 0.83$ (Planck Collaboration 2016).

2 METHODOLOGY

2.1 Modeling the ultraviolet luminosity functions

To model the UV LFs, we use the simple astrophysical galaxy model of Park et al. (2019) that ties galaxy properties to host halo masses via empirical scaling relations. Specifically, we assume that the typical stellar ($M_\star$) to halo mass (M_h) relation of faint galaxies is characterized by a *single power law (PL)*:

$$M_\star = f_\star \left(\frac{\Omega_\mathrm{b}}{\Omega_\mathrm{m}}\right) M_\mathrm{h}, \tag{1}$$

with

$$f_\star(M_\mathrm{h}) = f_{\star 10} \left(\frac{M_\mathrm{h}}{10^{10}\,\mathrm{M}_\odot}\right)^{\alpha}. \tag{2}$$

[2]Throughout this paper, we assume WDM in the form of thermal relics for simplicity. Nevertheless, this approach can be applied for other DM models that predict the suppression of small-scale structures, e.g. ultra-light DM (see e.g. Hu, Barkana & Gruzinov 2000; Marsh & Silk 2014; Marsh 2016; Schive et al. 2016), interacting DM, etc. (see e.g. Bœhm et al. 2002; Wilkinson, Bœhm & Lesgourgues 2014; Schaeffer & Schneider 2021). Furthermore, despite the fact that the ultra-light fuzzy DM transfer function has a different shape from that of thermal relic WDM (see e.g. Hu et al. 2000), constraints on the WDM mass may be converted to those of the fuzzy DM particle mass, (see e.g. Marsh 2016; Armengaud et al. 2017).

The typical star formation rate (SFR) of a galaxy hosted by a halo with mass M_h is then expressed as

$$\dot{M}_\star = \frac{M_\star}{t H^{-1}(z)}, \tag{3}$$

where t is dimensionless parameter which lies between 0 and 1, and $H(z)$ is the Hubble parameter. The SFR and UV luminosity are related by $\dot{M}_\star = \kappa_\mathrm{UV} L_\mathrm{UV}$, where $\kappa_\mathrm{UV} = 1.15 \times 10^{-28}\,\mathrm{M}_\odot\mathrm{yr}^{-1}\,\mathrm{ergs}^{-1}\,\mathrm{s}^{-1}\,\mathrm{Hz}^{-1}$ is a constant determined by the stellar initial mass function (e.g. Sun & Furlanetto 2016). As L_UV is proportional to the product of κ_UV and $f_\star$, the uncertainty in κ_UV can in practice be subsumed by the much larger uncertainty in the star formation efficiency parameter. The absolute magnitude M_UV is related to the UV luminosity with $M_\mathrm{UV} = 20.65 - 2.5\log_{10}\frac{L_\mathrm{UV}}{\mathrm{Hz}^{-1}\mathrm{ergs}^{-1}}$.

Given the above, the UV LF can be constructed from the halo mass function (HMF; $\mathrm{d}n/\mathrm{d}M_\mathrm{h}$) with:

$$\phi_\mathrm{UV} = f_\mathrm{duty} \frac{\mathrm{d}n}{\mathrm{d}M_\mathrm{h}} \frac{\mathrm{d}M_\mathrm{h}}{\mathrm{d}M_\mathrm{UV}}, \tag{4}$$

where f_duty describes the suppression of star formation in haloes smaller than some characteristic scale M_t set by inefficient gas cooling, photo-heating of gas and/or SNe feedback (see e.g. Okamoto, Gao & Theuns 2008; Sobacchi & Mesinger 2013a, b; Dayal et al. 2014; Yue, Ferrara & Xu 2016; Ocvirk et al. 2020):

$$f_\mathrm{duty} = \exp\left(-\frac{M_\mathrm{t}}{M_\mathrm{h}}\right). \tag{5}$$

Here, M_t is the characteristic mass scale of the suppression.

Because the normalization of the stellar-to-halo mass relation and the characteristic star formation time-scale are degenerate when computing the SFR (cf. equation 3), we will define their ratio as $r_s \equiv f_{\star,10}/t_\star$. Therefore this simple UV LFs model has only three free parameters:

(i) $r_s \equiv f_{\star,10}/t_\star$ – the ratio of the stellar fraction in $10^{10}\,\mathrm{M}_\odot$ haloes and the characteristic star formation time-scale (normalized by the Hubble time),

(ii) $\alpha_\star$ – the power law index of the stellar-to-halo mass relation,

(iii) M_t – the characteristic turnover halo mass scale below which star formation is exponentially suppressed.

Although simple, this three parameter model can reproduce current high-z LF observations (Oesch et al. 2018; Park et al. 2019; Bouwens et al. 2021). Below we use this as our default astrophysical model. Both semi-analytic models and hydrodynamic simulations show that similar, simple power-law scaling relations capture the average properties of the high-redshift, faint galaxies of interest to us (see Behroozi, Wechsler & Conroy 2013; Moster, Naab & White 2013; Mutch et al. 2016; Sun & Furlanetto 2016; Tacchella et al. 2018; Behroozi et al. 2019; Yung et al. 2019).

To check the robustness of our analysis, apart from the single power-law, we also consider a more complicated, *double power law (DPL)* star formation efficiency:

$$f_\star = \frac{f_{\star\mathrm{c}}}{2}\left[\left(\frac{M_\mathrm{h}}{M_\mathrm{c}}\right)^{\alpha_1} + \left(\frac{M_\mathrm{h}}{M_\mathrm{c}}\right)^{\alpha_2}\right]. \tag{6}$$

The motivation for this DPL is twofold.[3] end of the LF ($M_\mathrm{UV} >$ -20), where the putative suppression of haloes in WDM cosmologies

[3]Note that our DPL differs from the DPL scaling used to characterize a turnover in the star formation efficiency in massive galaxies, commonly attributed to AGN feedback (e.g. Moster et al. 2013; Mirocha, Furlanetto & Sun 2017; Tacchella et al. 2018). Here, we are only interested in the faint.

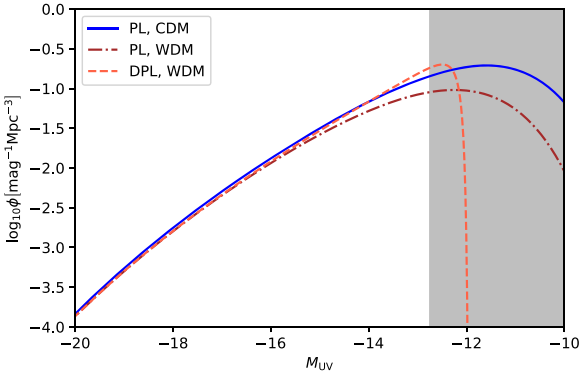

Figure 1. Examples of UV LFs from our models at z = 6. All cases assume inefficient star formation below a characteristic mass scale of $M_{\rm t} = 10^9$ M$_\odot$. The solid line corresponds to our fiducial single-power law model (PL) for the stellar to halo mass relation and a CDM cosmology. The dot–dashed and dashed lines correspond to WDM with $m_x = 3$ keV; however, the latter uses a more complicated DPL parametrization for the stellar to halo mass relation. The shaded region corresponds to the magnitudes which are not probed by *HST* observations. This example illustrates that an increase in star formation efficiency for faint galaxies can partially compensate for the decrease in galaxy number in WDM cosmologies over the observable range; however, the Bayesian evidence could penalize the red curve compared to the blue, due to its larger effective prior volume.

would be most pronounced. Current observations and theoretical models find that these faint galaxies are accurately characterized with a single power law, i.e. our PL model. First, some theoretical and empirical models suggest that the top-heavy initial mass function of primordial, molecularly cooled galaxies could result in an enhanced emissivity (see e.g. Mirocha & Furlanetto 2019; Qin et al. 2020 and references therein). This would effectively steepen the faint end of the LF, since the UV magnitudes of primordial galaxies would overlap with those of more evolved galaxies. However, some of these models were tuned to reproduce controversial observations (e.g. Livermore, Finkelstein & Lotz 2017; Bowman et al. 2018), and the *a priori* motivation of the DPL is dubious. For example, if the EDGES signal (Bowman et al. 2018) is of cosmic origin, its timing would have to imply an enhanced emissivity in non-standard, faint galaxies (Mirocha & Furlanetto 2019; Qin et al. 2020).

Instead, the main reason for including the DPL in this study is its additional flexibility. The DPL allows a higher star formation efficiency in galaxies hosted by small DM haloes, which could partially compensate for a dearth in their number density in WDM scenarios. An example of this is shown in Fig. 1. Here, the DPL WDM model denoted by the dashed curve mimics the (simpler) PL CDM model shown by the blue curve over the magnitude range probed by current observations. The increased luminosity of the faint galaxies in the DPL model effectively moves them over to the left in this plot, resulting in the evident up-turn in the LF at $M_{\rm UV} > -15$ and a sharp cutoff beyond $M_{\rm UV} > -12$.

Even for CDM, we do not know the shape of the inevitable turn-over in the star formation efficiency at the faint end, and the DPL allows for additional flexibility;however, this flexibility comes at the cost of two additional parameters: a second power-law index and the transition scale, $M_{\rm c}$.

Finally, we note that in Appendix A we also show results using a redshift dependent stellar-to-halo mass relation. Consistent with previous work (Oesch et al. 2018; Park et al. 2019; Bouwens et al. 2021), we find that current data does not favour a redshift dependence of f_*.

2.2 Halo mass function

The HMF is defined as

$$\frac{{\rm d}n}{{\rm dln}M_{\rm h}} = f(\nu)\frac{\rho_m}{M_{\rm h}}\frac{{\rm dln}\sigma^{-1}}{{\rm dln}M_{\rm h}}, \tag{7}$$

where $\nu = \left(\frac{\delta_c^2(z)}{\sigma^2}\right)$, $\delta_c(z) = \frac{1.686}{D(z)}$, $D(z)$ is the growth factor (Heath 1977), $\sigma^2(M)$ is the mass variance on scale M and $\bar{\rho}_m$ is the mean matter density of the Universe. In WDM cosmologies, the HMF cannot be analytically derived from the first principles. However, N-body simulations show good agreement with analytic HMFs using modified transfer functions, over the range $\sim 10^{11} - \sim 10^9$ M$_\odot$ probed by current LF observations (e.g. Schneider 2015; Bose et al. 2016). Motivated by these results, we use the ellipsoidal collapse parametrization (Sheth & Tormen 2002)

$$f(\nu) = A_{\rm ST}\sqrt{\frac{2q\nu}{\pi}}\left(1 + (q\nu)^{-p}\right){\rm e}^{-q\nu/2}, \tag{8}$$

with $A_{\rm ST} = 0.322$, $p = 0.3$, $q = 1$ and $\nu = \frac{\delta_c^2(z)}{\sigma^2(M)}$.[4]To calculate σ, we use a sharp k-space filter, which is in a good agreement with the results of N-body simulations, over the relevant halo mass range (Benson et al. 2013; Schneider 2015; Bose et al. 2016):

$$\sigma^2(M) = \int P(k)\theta(1 - kR){\rm d}^3k, \tag{9}$$

where $M_{\rm h}(R) = \frac{4\pi}{3}\left(\frac{R}{a}\right)^3$ and $\theta(x)$ is the Heaviside step function. Following Schneider (2015), we choose $a = 2.5$.

The warm DM power spectrum is connected to the CDM one via the transfer function $T(k)$:

$$P_{\rm WDM}(k) = P_{\rm CDM}(k)T^2(k). \tag{10}$$

We use the transfer function parametrization from Viel et al. (2005):

$$T^2(k) = (1 + (bk)^{2\mu})^{-10/\mu}, \tag{11}$$

where

$$b = 0.049\left(\frac{m_{\rm x}}{1{\rm kev}}\right)^{-1.11}\left(\frac{\Omega_{\rm WDM}}{0.25}\right)^{0.11}\left(\frac{h}{0.7}\right)^{1.22}h^{-1}{\rm Mpc}, \tag{12}$$

$\mu = 1.12$, and $m_{\rm x}$ is the mass of the DM particle (in keV).[5]We use HMF package for generation of halo mass functions (Murray, Power & Robotham 2013)

2.3 Data analysis

We use a likelihood function of the following form:

$$P(D|\theta, \mathcal{M}) = \prod_{M_{\rm UV}\ {\rm bins}} S\left(x(\theta, \mathcal{M}), \bar{x}_{\rm obs}, \sigma_1, \sigma_2\right), \tag{13}$$

[4]We confirm that our conclusions are unchanged using alternate values of the parameters, see Appendix B.

[5]Strictly speaking, CDM also has a cut-off scale, which corresponds to a much shorter streaming length than WDM. However, this scale is far too small to impact the observations under consideration. Since our cosmological model is tied to the observations via the matter power spectrum, and WDM requires adjusting an additional turn-over scale to match the data, there is an Occam's razor penalty in the Bayesian evidence for WDM compared to CDM.

Table 1. The parameters of the models, used in this paper, and corresponding prior distributions.

Parameter	Allowed range	Units	Prior
r_s	0.01–100	–	Flat log
$\alpha, \alpha_1, \alpha_2$	−1.0–1.0	–	Flat linear
M_t, M_c	10^8–10^{10}	$M_\odot$	Flat log
$1/m_x$	0–1	keV^{-1}	Flat linear

where $x(\theta, \mathcal{M}) = \log_{10}\phi_{pred}(\theta, M)$ is the predicted value of the decimal logarithm of the UV LF in the model $\mathcal{M}$, $\bar{x}_{obs}$ is the observational value, σ_1 and σ_2 are positive and negative errors. To account for asymmetric error bars, we take $S(x, \bar{x}_{obs}, \sigma_1, \sigma_2)$ to have a split-norm distribution (cf. Gillet, Mesinger & Park 2020):

$$S(x, \bar{x}_{obs}, \sigma_1, \sigma_2) = \begin{cases} A\exp\left(-\dfrac{(x-\bar{x}_{obs})^2}{2\sigma_1^2}\right), & x > \bar{x}_{obs}, \\ A\exp\left(-\dfrac{(x-\bar{x}_{obs})^2}{2\sigma_2^2}\right), & x \le \bar{x}_{obs}. \end{cases} \quad (14)$$

Here, $A = \frac{1}{\sqrt{2\pi}}\frac{2}{\sigma_1+\sigma_2}$ is the normalization constant.

If we assume a single power-law $f_\star$ dependency on halo mass (model PL), the astrophysical model includes three free parameters: r_s, α, and M_t. In case of DPL, the UV LF model includes five parameters, namely r_s, α_1, α_2, M_c, and M_t. In thermal relic WDM cosmologies, the matter power spectrum has an additional cut-off scale parametrized by the WDM mass m_x. As there is no reliable upper limit on the WDM mass, we adopt the inverse quantity $1/m_x$ as the free parameter.[6] The upper limit on this parameter arises from the lowest allowed value of m_x, which we choose to be $m_x = 1$ keV following numerous studies of structure formation (see e.g. most of the bounds summarized in tables 3 and 4 of Enzi et al. 2021). Our assumptions about the ranges of the values of model parameters and prior probability distributions are listed in Table 1.

We analyse the following data sets obtained via *Hubble Space Telescope (HST)* observations:

(i) the 'A18' data set comprises UV LF data from Atek et al. (2018) for $z \approx 6$ based on the analysis of the observations of the six clusters: Abell 2744, MACS0416, MACS0717, MACS1149, AS1063, and A370 during the *Hubble Frontier Field* program;

(ii) the 'B17' data set is UV LF data from Bouwens et al. (2017) for $z \approx 6$ based on the four *HFF* clusters: Abell 2744, MACS0416, MACS0717, and MACS1149;

(iii) the 'B + ' is 'B17' data set at $z \approx 6$ plus data from Bouwens et al. (2015) for $z = 7$, 8 obtained from XDF, HUDF09-Ps, ERS, BoRG/HIPPIES, and CANDELS *HST* fields;

(iv) the auxiliary 'all data' data set corresponding to a concatenation of 'A18' and 'B + '.

The galaxy samples of the 'B17', 'B + ', and 'A18' data sets were obtained via colour selection criteria (see more details in Bouwens et al. 2015, 2017; Atek et al. 2018). The shape of the observational UV LF depends on the assumed source size distribution and gravitational lens model (see e.g. Bouwens et al. 2015; Atek et al. 2018). While the UV LFs at $z = 6$ and $M_{UV} \lesssim -15$ are similar (see e.g. Atek et al. 2018), the difference in assumed models leads to very different shapes of the UV LFs at $M_{UV} \gtrsim -15$. As our constraints on WDM mass strongly depend on this ultra-faint part of UV LF, we also introduce the auxiliary 'all data' data set. By combining 'A' and 'B + ' data sets, we hope to roughly average over the differences in the systematics that drive their very different UV LF shapes at $M_{UV} > -15$. We shall see below, however, that our constraints are not particularly sensitive to the choice of data set, due to the large quoted error bars at these ultra-faint magnitudes.

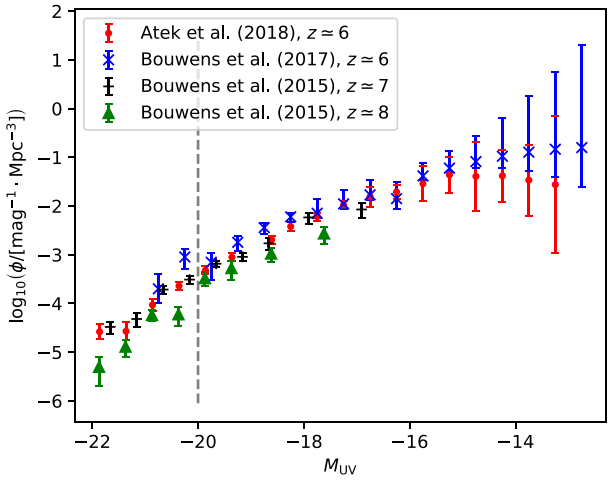

Figure 2. 'A18' and 'B + ' data sets. At $z = 6$, the 'B17' and 'B + ' data sets are the same. The dashed line shows the cut at magnitude −20 (see main text).

The corresponding data points are shown in Fig. 2. Note that, by adding higher redshifts in the B + data set, we can probe also the redshift evolution of the LFs, which could better discriminate WDM and CDM (Dayal et al. 2015; Khimey et al. 2020). The 'all data' data set equally weighs all observational data points in all of the data sets (see e.g. Finkelstein 2016 for a similar approach).[7]

Our model of UV LF does not take into account the effects of AGN feedback nor dust extinction. Therefore, we do not include data points with magnitudes lower than −20 focusing instead on the faint end that is most sensitive to WDM (cf. Fig. 1). Indeed, both observations and simulations suggest that dust attenuation is negligible at $M_{UV} > -20$ for the high redshifts of interest here (e.g. Bouwens et al. 2014; Wilkins et al. 2017; Ma et al. 2019; Vijayan et al. 2021). Similarly, the impact of AGN feedback should be small on these magnitudes (see e.g. Yung et al. 2020).

We use the Bayes factor $K_{21} = \frac{P(M_2|D)}{P(M_1|D)}$ for model comparison. According to the Bayes theorem, the posterior probability of the model M_i is defined as:

$$P(M_i|D) = \frac{P(D|M_i)P(M_i)}{P(D)}, \quad (15)$$

therefore the Bayes factor could be expressed as a ratio of marginal-

[6]We also repeat our analysis with a flat prior over the range $m_x = 1$–5 keV, as well as $m_x = 1$–10 keV. We find that our model comparison results and derived 95 per cent m_x constraints are unchanged by these alternate choices of prior.

[7]Note, that the 'all data' data set includes the pairs of data points with the same magnitudes at $z = 6$ from the 'A18' and 'B + ' data sets, respectively. Each 'duplicated' data point can be interpreted as a one data point with shrunk error bars and shifted mean. There is a concern about the appropriateness of the Bayesian model comparison based on the data set with underestimated error bars. Therefore, we don't calculate the Bayesian evidences for 'all data' data set.

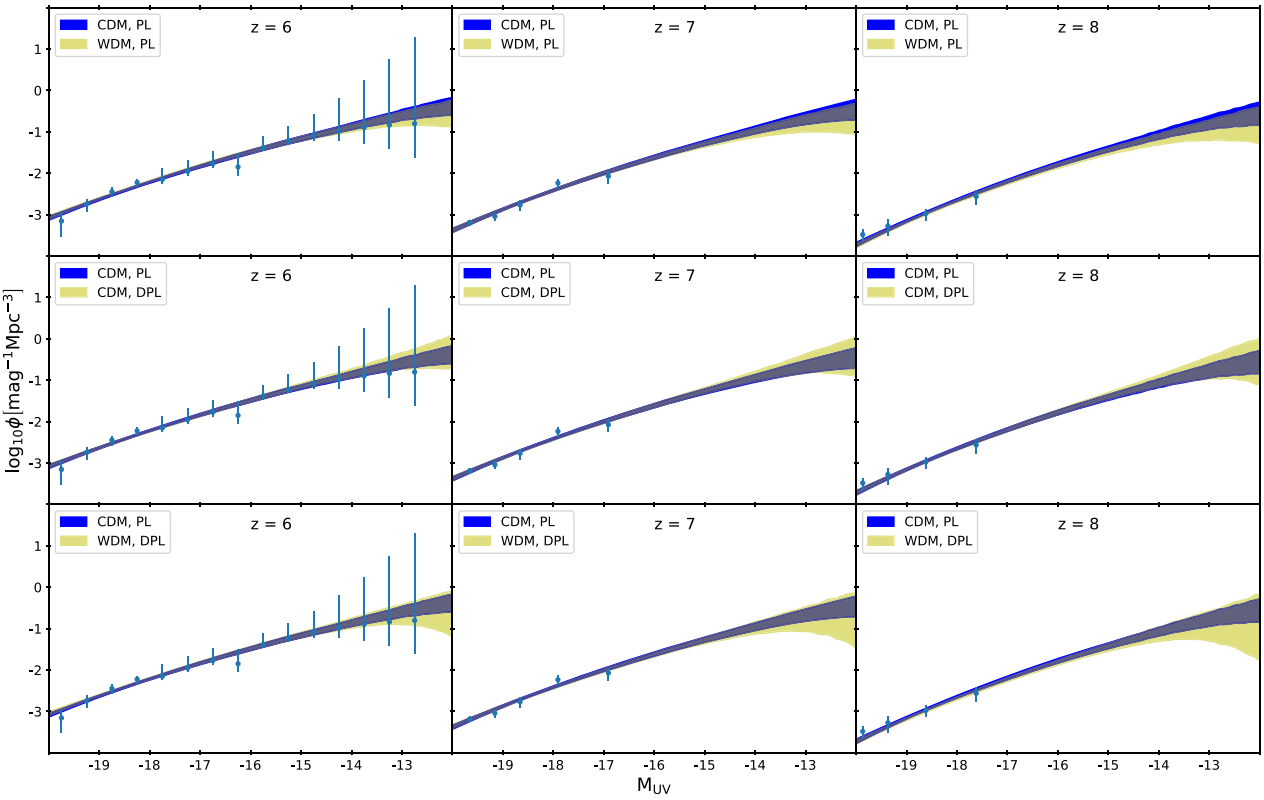

Figure 3. The 68 per cent C.L. of the UV LF posteriors for all models, computed using the 'B+' data set (blue points with error bars). Different redshifts are shown in columns, while rows correspond to different astrophysical and DM models. For reference, the simplest PL + CDM model is shown in blue in all panels. As expected, the posteriors of models with larger prior volumes (more free parameters) are broader, though the differences are only evident at $M_{\rm UV} > -15$.

ized likelihoods (evidences):

$$K_{21} = \frac{P(D|M_2)}{P(D|M_1)}, \tag{16}$$

assuming equal model priors $P(M_1) = P(M_2)$. The model M_2 can be considered to be substantially supported if $\log_{10}K_{21} > 1/2$ and strongly supported if $\log_{10}K_{21} > 1$ (Kass & Raftery 1995).

For each of the models under consideration, we calculate the marginalized likelihood

$$P(D|M_i) = \int p(D|\theta, M_i)\pi(\theta|M_i)\mathrm{d}\theta, \tag{17}$$

where $p(D|\theta, M_i)$ is the likelihood function and $\pi(\theta|M_i)$ are prior distributions of the parameters of the model M_i. The calculations are done by using dynamical nested sampling method (Higson et al. 2019) implemented in the DYNESTY PYTHON package (Speagle 2020). We also perform Markov chain Monte Carlo (MCMC) sampling using the affine-invariant ensemble sampler implemented in the EMCEE code (Foreman-Mackey et al. 2013).

3 RESULTS

3.1 Model comparison

As an illustration of the procedure, in Fig. 3, we show the 68 per cent C.L. of the marginalized LFs posteriors for each model (see Appendix C for the corresponding corner plots of the model parameters), using the 'B + ' data set. Columns correspond to different redshifts, while different astro/cosmo models are shown with the yellow shaded regions in the rows. In all panels, the simplest (CDM, PL) model is shown in blue.

Table 2. Base 10 logarithm of the Bayes factor for various DM scenarios and star formation efficiency models, with respect to the simplest (PL, CDM) model, M_1. Top rows of the table indicate the model M_2.The modest evidence ratios only allow for weak model preferences.

	CDM		WDM	
	PL	DPL	PL	DPL
'A18'	0	0.14 ± 0.09	0.05 ± 0.09	0.05 ± 0.08
'B17'	0	0.08 ± 0.08	-0.33 ± 0.09	-0.26 ± 0.09
'B + '	0	0.29 ± 0.09	-0.33 ± 0.1	-0.06 ± 0.1

The recovered LFs at the brighter end ($M_{\rm UV} < -15$) are comparable for all models considered. However, the LF posterior is broader at $M_{\rm UV} > -15$ for more complicated models (larger prior volume). This is especially evident in the bottom row, corresponding to the DPL + WDM model that has the most free parameters. For example, at $M_{\rm UV} \gtrsim -13$, the DPL + WDM 68 per cent C.L. are wider by factors of $\gtrsim$2.

How does their evidence compare? We perform inference using all combinations of models and observational data sets. The resulting Bayes factors are summarized in Table 2, relative to the simplest CDM + PL model. This table represents the main result of this work.

Unfortunately, we find that no Bayes factor is large enough to be used for conclusive model selection. The CDM model is slightly

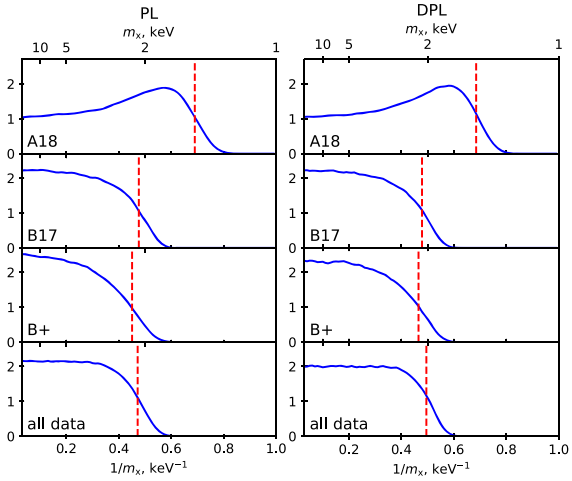

Figure 4. Marginalized posterior probability densities of $1/m_x$ for 'power-law' and 'DPL' models of $f_\star$ and different data sets. Dashed lines denote the 95 per cent credible limits.

Table 3. 95% lower bounds (in keV) on the mass of thermal relic WDM particle resulting from different data sets and model choices.

Model	WDM m_x/keV bound, 95% C.L. Data set			
	'A18'	'B17'	'B + '	'All data'
PL	1.5	2.1	2.2	2.1
DPL	1.5	2.1	2.1	2.0

preferred by the 'B17' and 'B + ' data sets, but the corresponding Bayes factor $K \simeq 2$ is not enough to substantially support CDM against WDM. Interestingly, the 'B+' data set substantially prefers CDM + DPL over WDM + PL; however, $\log_{10} \frac{P(D|\,\mathrm{CDM,\,DPL})}{P(D|\,\mathrm{WDM,\,PL})} \simeq 0.6$ is very close to the lower level of Bayes factor required for substantial support of the model.

3.2 Constraining the WDM particle mass

Given that we cannot rule out WDM using current LFs, we now look at the particle mass constraints in each of the WDM models. The marginalized 1D posteriors of $1/m_x$ for all WDM models and data sets are shown in Fig. 4. The 95 per cent C.L. are denoted by the vertical dashed lines are reported in Table 3. Due to its suggestive flattening of the faint-end slope (cf. Fig. 2), the 'A18' data set has the weakest limit: $m_x > 1.5$ keV. All other data sets, including the all data one, result in $m_x \gtrsim 2$ keV. Interestingly, the constraints using PL and DPL are comparable. This is likely do to the fact that the increased SFRs allowed by the DPL model can only modestly compensate for the dearth of haloes in WDM; however, this occurs over the magnitude range where the observational error bars are very large (cf. Figs 1and 2). For $m_x \lesssim 2$ keV the dearth of haloes is dramatic in the magnitude ranges probed by current observations, and cannot be compensated by astrophysics even in the DPL parametrization.

Understandably, we also find a strong degeneracy between $1/m_x$ and the astrophysical turn-over scale M_t (see Figs C1 and C2). This is qualitatively consistent with previous works (Dayal et al. 2017; Villanueva-Domingo et al. 2018; Esmerian & Gnedin 2021; Khimey et al. 2020) that found a strong degeneracy between astrophysics and cosmology using currently available LFs. The posteriors demonstrate that the constraints on both the WDM particle mass and turn-over mass mostly come from $z = 6$ data, which goes to the faintest magnitudes. The addition of the higher redshift data mostly tightens constraints on parameters responsible for the bright end of the LFs.

3.3 How will limits improve with JWST?

Future observations with the *James Webb Space Telescope (JWST)* should probe fainter magnitudes than currently available with *HST*. This should facilitate tighter DM constraints (e.g. Dayal et al. 2015; Lapi & Danese 2015).

To quantify this, we repeat our analysis using the CDM + PL and WDM + PL models on the simulated *JWST* UV LF observations from Park et al. (2020; specifically their *JWST*-F data set). These authors use the results of hydrodynamic simulations in CDM cosmology that agree with current data, but provide predictions at magnitudes too faint to be currently observed with *HST*. *JWST* faint end uncertainties were simply estimated by shifting the current *HST* error bars 1.5 mag deeper (see Park et al. 2020 and references therein for more details).

We find that this *JWST* mock observation supports CDM over WDM with a Bayes factor of $\simeq$3, which is still not sufficient for a robust distinction between the models. We also find that the 95 per cent C.L. lower bound on the WDM mass increases to 2.5 keV. Our results are in agreement with Khimey et al. (2020).

4 COMPARISON WITH EXISTING WDM CONSTRAINTS

It is useful to place our WDM particle mass limits in context with other limits. Several approaches have been applied to constrain WDM using UV LFs. The most model-independent approach was suggested by Pacucci et al. (2013): comparing the cumulative galaxy number to the cumulative halo number. This approach is only dependent on the assumed HMF, and is conservative since it does not depend on how UV luminosity is assigned to DM haloes. Pacucci et al. (2013) initially quoted a limit of $m_x > 1$ keV based on preliminary results from the CLASH survey (see also Schultz et al. 2014; Menci et al. 2016a, b, 2017). Subsequent work suggested a 2.4 keV 2σ lower bound (Menci et al. 2016b) using the LFs from Livermore et al. (2017). Our constraint is somewhat weaker than this because the faint-end of the Livermore et al. (2017) LFs are systematically higher than the data sets used in this work. Alternatively, Corasaniti et al. (2017) modeled the UV LFs in WDM, fitting the data from Atek et al. (2015), Bouwens et al. (2015), and Bouwens et al. (2017). Their 1.5 keV lower bound is somewhat weaker than ours, possibly due to the different assumed HMFs.

Tighter 3–5 keV 2σ lower limits on the WDM mass were obtained from the analysis of small-scale structure in the Lyman-α forest (see e.g. Viel et al. 2013; Baur et al. 2016; Iršič et al. 2017). These constraints require marginalizing over the thermal and ionization history of the IGM. More recent, conservative assumptions on these histories resulted in a weaker $\sim$2 keV (2σ) limit Garzilli et al. (2019), which is the same as we find here using the UV LFs.

Even tighter 4–5 keV 2σ lower bounds are obtained from the analysis of flux ratios of the quadruply imaged quasars (Gilman et al. 2019, 2020). However, these lower bounds are strongly dependent on the choice of prior (see section 4.2 in Enzi et al. 2021). To overcome this difficulty, Gilman et al. (2020), Enzi et al. (2021), and Nadler et al. (2021b) used marginalized likelihoods ratios to obtain somewhat weaker lower limits: 3–4 keV in (Gilman et al. 2020); and 2.55 keV from the joint analysis of Lyman-α, MW satellites, and gravitational lensing in Enzi et al. (2021). The recent work of Nadler

et al. (2021b) rejects $\lesssim 7.4$ keV masses with marginalized likelihood ratio between such WDM and CDM $\lesssim 1/20$ (roughly corresponding to the 2σ bound) from the joint analysis of MW satellites and strong gravitational lensing. Moreover, 2.5 keV WDM masses are strongly rejected with a likelihood ratio $>1/100$ (see fig. 6 of Nadler et al. 2021b). It should be noted, that these constraints are strongly dependent on the sub-HMF. There is some concern that previously proposed fits of sub-HMFs, used in these works, underestimate the number of satellites (Lovell 2020). Furthermore, recent MW satellite analysis by Newton et al. (2020) gives a a weaker but less model-dependent lower limit of $\sim$2 keV (when marginalizing over baryonic feedback) and a stronger but model-dependent lower limit of 3–4 keV (when modeling the baryonic feedback).

5 CONCLUSIONS

The abundances and brightness of early galaxies depend both on the unknown DM properties and the poorly constrained physics of star formation. The degeneracy between astrophysics and cosmology is always a bottle-neck when constraining DM models with a dearth of small-scale power, such as WDM.

In this paper, we apply Bayesian inference to the analysis of UV LFs at redshifts 6–8, varying prescriptions for both the DM and star formation. We adopt two flexible astrophysical models, using a single and a DPL to characterize the stellar-to-halo mass relation. For each astrophysical model, we also assume either CDM or thermal relic WDM when computing halo abundances.

We compute the Bayes factor between the models and find no substantial preference for any model, using current UV LFs. CDM is only weakly favoured over. We also conclude that our fiducial model (CDM with a simple redshift-independent power-law star-formation efficiency for faint galaxies) describes the existing UV LF data well.

We find that in WDM cosmologies, particle masses of $\lesssim 2$ keV are rejected with a 95 per cent credible level using only the UV LFs. This result is consistent with other astrophysical limits on the particle mass. Using a mock *JWST* data set from Park et al. (2020), we forecast that this limit could improve to $\sim$2.5 keV with upcoming *JWST* observations.

Our work showcases how Bayesian model comparison can be applied to reionization-era observations to discriminate against needlessly complicated astrophysics that can mimic cosmology. In the future, we will apply this framework to upcoming 21-cm interferometric observations of the Epoch of Reionization and Cosmic Dawn. Although galaxy astrophysics can be 'tuned' to mimic a 21-cm WDM signal, such tuning is likely very ad hoc (see for example fig. 5 in Sitwell et al. 2014). Indeed, Muñoz, Dvorkin & Cyr-Racine (2020) and Jones et al. (2021) use a simpler SFR prescription and Fisher forecasts to suggest that upcoming interferometers would be able to constrain warm and fuzzy DM, respectively. It is also encouraging that Muñoz et al. (2021) predict dark-acoustic oscillations will also be detectable with 21-cm data. The enormous data set provided by upcoming 21-cm observations with the Hydrogen Epoch of Reionization Array (HERA) and Square Kilometer Array (SKA) will be very constraining, facilitating detailed model selection (Binnie & Pritchard 2019; Qin et al. 2021).

ACKNOWLEDGEMENTS

We thank R. Trotta, A. Pilipenko, M. Viel, and J. Muñoz for helpful comments and discussions. AR and DS acknowledge support from the National Academy of Sciences of Ukraine by its priority project No.0120U100935 'Fundamental properties of the matter in the relativistic collisions of nuclei and in the early Universe'. The work of AR was also partially supported by the ICTP through AF-06. AM acknowledges funding from the European Research Council (ERC) under the European Union's Horizon 2020 research and innovation programme (grant agreement No 638809 - AIDA). The results presented here reflect the authors' views; the ERC is not responsible for their use. The calculations presented here were performed on the BITP computer cluster.

DATA AVAILABILITY

The LFs underlying this article are publicly available. The code that supports the findings of this study will be shared on reasonable request to the corresponding author.

REFERENCES

Adhikari R. et al., 2017, J. Cosmol. Astropart. Phys., 025
Armengaud E., Palanque-Delabrouille N., Yèche C., Marsh D. J. E., Baur J., 2017, MNRAS, 471, 4606
Atek H. et al., 2015, ApJ, 800, 18
Atek H., Richard J., Kneib J.-P., Schaerer D., 2018, MNRAS, 479, 5184
Banik N., Bovy J., Bertone G., Erkal D., de Boer T. J. L., 2019, preprint (arXiv:1911.02663)
Baur J., Palanque-Delabrouille N., Yèche C., Magneville C., Viel M., 2016, J. Cosmol. Astropart. Phys., 2016, 012
Baur J., Palanque-Delabrouille N., Yeche C., Boyarsky A., Ruchayskiy O., Armengaud E., Lesgourgues J., 2017, J. Cosmol. Astropart. Phys., 2017, 013
Behroozi P. S., Wechsler R. H., Conroy C., 2013, ApJ, 770, 57
Behroozi P., Wechsler R. H., Hearin A. P., Conroy C., 2019, MNRAS, 488, 3143
Benson A. J. et al., 2013, MNRAS, 428, 1774
Binnie T., Pritchard J. R., 2019, MNRAS, 487, 1160
Birrer S., Amara A., Refregier A., 2017, J. Cosmol. Astropart. Phys., 2017, 037
Bose S., Hellwing W. A., Frenk C. S., Jenkins A., Lovell M. R., Helly J. C., Li B., 2016, MNRAS, 455, 318
Bouwens R. J. et al., 2014, ApJ, 793, 115
Bouwens R. J. et al., 2015, ApJ, 803, 34
Bouwens R. J., Oesch P. A., Illingworth G. D., Ellis R. S., Stefanon M., 2017, ApJ, 843, 129
Bouwens R. J. et al., 2021, AJ, 162, 47
Bowman J. D., Rogers A. E. E., Monsalve R. A., Mozdzen T. J., Mahesh N., 2018, Nature, 555, 67
Boyarsky A., Ruchayskiy O., Iakubovskyi D., Franse J., 2014, Phys. Rev. Lett., 113, 251301
Boyarsky A., Drewes M., Lasserre T., Mertens S., Ruchayskiy O., 2019, Prog. Part. Nucl. Phys., 104, 1
Boyarsky A., Malyshev D., Ruchayskiy O., Savchenko D., 2021, SciPost Astro. Core, 1, 1
Bulbul E., Markevitch M., Foster A., Smith R. K., Loewenstein M., Randall S. W., 2014, ApJ, 789, 13
Bullock J. S., Boylan-Kolchin M., 2017, ARA&A, 55, 343
Bœhm C., Riazuelo A., Hansen S. H., Schaeffer R., 2002, Phys. Rev. D, 66, 083505
Corasaniti P. S., Agarwal S., Marsh D. J. E., Das S., 2017, Phys. Rev. D, 95, 083512
Dayal P., Ferrara A., Dunlop J. S., Pacucci F., 2014, MNRAS, 445, 2545
Dayal P., Mesinger A., Pacucci F., 2015, ApJ, 806, 67
Dayal P., Choudhury T. R., Bromm V., Pacucci F., 2017, ApJ, 836, 16
de Souza R. S., Mesinger A., Ferrara A., Haiman Z., Perna R., Yoshida N., 2013, MNRAS, 432, 3218
Dessert C., Rodd N. L., Safdi B. R., 2020, Science, 367, 1465
Enzi W. et al., 2021, MNRAS, 506, 5848
Esmerian C. J., Gnedin N. Y., 2021, ApJ, 910, 117

Finkelstein S. L., 2016, Publ. Astron. Soc. Aust., 33, e037
Foreman-Mackey D., Hogg D. W., Lang D., Goodman J., 2013, PASP, 125, 306
Garzilli A., Ruchayskiy O., Magalich A., Boyarsky A., 2019, preprint (arXiv:1912.09397)
Gillet N. J. F., Mesinger A., Park J., 2020, MNRAS, 491, 1980
Gilman D., Birrer S., Treu T., Nierenberg A., Benson A., 2019, MNRAS, 487, 5721
Gilman D., Birrer S., Nierenberg A., Treu T., Du X., Benson A., 2020, MNRAS, 491, 6077
Heath D. J., 1977, MNRAS, 179, 351
Higson E., Handley W., Hobson M., Lasenby A., 2019, Stat. Comput., 29, 891
Hsueh J. W., Enzi W., Vegetti S., Auger M. W., Fassnacht C. D., Despali G., Koopmans L. V. E., McKean J. P., 2020, MNRAS, 492, 3047
Hu W., Barkana R., Gruzinov A., 2000, Phys. Rev. Lett., 85, 1158
Iršič V. et al., 2017, Phys. Rev. D, 96, 023522
Jethwa P., Erkal D., Belokurov V., 2018, MNRAS, 473, 2060
Jones D., Palatnick S., Chen R., Beane A., Lidz A., 2021, ApJ, 913, 7
Kass R. E., Raftery A. E., 1995, J. Am. Stat. Assoc., 90, 773
Kennedy R., Frenk C., Cole S., Benson A., 2014, MNRAS, 442, 2487
Khimey D., Bose S., Tacchella S., 2021, MNRAS, 506, 4139
Kim S. Y., Peter A. H. G., Hargis J. R., 2018, Phys. Rev. Lett., 121, 211302
Klypin A., Kravtsov A. V., Valenzuela O., Prada F., 1999, ApJ, 522, 82
Lapi A., Danese L., 2015, J. Cosmol. Astropart. Phys., 2015, 003
Livermore R. C., Finkelstein S. L., Lotz J. M., 2017, ApJ, 835, 113
Lovell M. R., 2020, MNRAS, 493, L11
Ma X. et al., 2019, MNRAS, 487, 1844
Marsh D. J. E., 2016, Phys. Rep., 643, 1
Marsh D. J. E., Silk J., 2014, MNRAS, 437, 2652
Menci N., Sanchez N. G., Castellano M., Grazian A., 2016a, ApJ, 818, 90
Menci N., Grazian A., Castellano M., Sanchez N. G., 2016b, ApJ, 825, L1
Menci N., Merle A., Totzauer M., Schneider A., Grazian A., Castellano M., Sanchez N. G., 2017, ApJ, 836, 61
Mirocha J., 2020, MNRAS, 499, 4534
Mirocha J., Furlanetto S. R., 2019, MNRAS, 483, 1980
Mirocha J., Furlanetto S. R., Sun G., 2017, MNRAS, 464, 1365
Moore B., Ghigna S., Governato F., Lake G., Quinn T., Stadel J., Tozzi P., 1999, ApJ, 524, L19
Moster B. P., Naab T., White S. D. M., 2013, MNRAS, 428, 3121
Muñoz J. B., Dvorkin C., Cyr-Racine F.-Y., 2020, Phys. Rev. D, 101, 063526
Muñoz J. B., Bohr S., Cyr-Racine F.-Y., Zavala J., Vogelsberger M., 2021, Phys. Rev. D, 103, 043512
Murgia R., Iršič V., Viel M., 2018, Phys. Rev. D, 98, 083540
Murray S. G., Power C., Robotham A. S. G., 2013, Astron. Comput., 3, 23
Mutch S. J., Geil P. M., Poole G. B., Angel P. W., Duffy A. R., Mesinger A., Wyithe J. S. B., 2016, MNRAS, 462, 250
Nadler E. O. et al., 2021a, Phys. Rev. Lett., 126, 091101
Nadler E. O., Birrer S., Gilman D., Wechsler R. H., Du X., Benson A., Nierenberg A. M., Treu T., 2021b, ApJ, 917, 7
Newton O. et al., 2021, J. Cosmol. Astropart. Phys., 2021, 062
Ocvirk P. et al., 2020, MNRAS, 496, 4087
Oesch P. A., Bouwens R. J., Illingworth G. D., Labbé I., Stefanon M., 2018, ApJ, 855, 105
Okamoto T., Gao L., Theuns T., 2008, MNRAS, 390, 920
Pacucci F., Mesinger A., Haiman Z., 2013, MNRAS, 435, L53
Park J., Mesinger A., Greig B., Gillet N., 2019, MNRAS, 484, 933
Park J., Gillet N., Mesinger A., Greig B., 2020, MNRAS, 491, 3891
Planck Collaboration, 2016, A&A, 594, A13
Polisensky E., Ricotti M., 2011, Phys. Rev. D, 83, 043506
Qin Y., Mesinger A., Park J., Greig B., Muñoz J. B., 2020, MNRAS, 495, 123
Qin Y., Mesinger A., Greig B., Park J., 2021, MNRAS, 501, 4748
Sabti N., Muñoz J. B., Blas D., 2021, J. Cosmol. Astropart. Phys., 2021, 010
Schaeffer T., Schneider A., 2021, MNRAS, 504, 3773
Schive H.-Y., Chiueh T., Broadhurst T., Huang K.-W., 2016, ApJ, 818, 89
Schneider A., 2015, MNRAS, 451, 3117
Schneider A., Smith R. E., Reed D., 2013, MNRAS, 433, 1573
Schultz C., Oñorbe J., Abazajian K. N., Bullock J. S., 2014, MNRAS, 442, 1597
Sheth R. K., Tormen G., 2002, MNRAS, 329, 61
Sitwell M., Mesinger A., Ma Y.-Z., Sigurdson K., 2014, MNRAS, 438, 2664
Sobacchi E., Mesinger A., 2013a, MNRAS, 432, L51
Sobacchi E., Mesinger A., 2013b, MNRAS, 432, 3340
Speagle J. S., 2020, MNRAS, 493, 3132
Sun G., Furlanetto S. R., 2016, MNRAS, 460, 417
Tacchella S., Bose S., Conroy C., Eisenstein D. J., Johnson B. D., 2018, ApJ, 868, 92
Trotta R., 2017, preprint (arXiv:1701.01467)
Vegetti S., Despali G., Lovell M. R., Enzi W., 2018, MNRAS, 481, 3661
Viel M., Lesgourgues J., Haehnelt M. G., Matarrese S., Riotto A., 2005, Phys. Rev. D, 71, 063534
Viel M., Becker G. D., Bolton J. S., Haehnelt M. G., 2013, Phys. Rev. D, 88, 043502
Vijayan A. P., Lovell C. C., Wilkins S. M., Thomas P. A., Barnes D. J., Irodotou D., Kuusisto J., Roper W. J., 2021, MNRAS, 501, 3289
Villanueva-Domingo P., Gnedin N. Y., Mena O., 2018, ApJ, 852, 139
Wilkins S. M., Feng Y., Di Matteo T., Croft R., Lovell C. C., Waters D., 2017, MNRAS, 469, 2517
Wilkinson R. J., Bœhm C., Lesgourgues J., 2014, J. Cosmol. Astropart. Phys., 2014, 011
Yoshiura S., Oguri M., Takahashi K., Takahashi T., 2020, Phys. Rev. D, 102, 083515
Yue B., Ferrara A., Xu Y., 2016, MNRAS, 463, 1968
Yung L. Y. A., Somerville R. S., Popping G., Finkelstein S. L., Ferguson H. C., Davé R., 2019, MNRAS, 490, 2855
Yung L. Y. A., Somerville R. S., Finkelstein S. L., Popping G., Davé R., Venkatesan A., Behroozi P., Ferguson H. C., 2020, MNRAS, 496, 4574

APPENDIX A: REDSHIFT-EVOLUTION OF STAR FORMATION EFFICIENCY

In this work, the base-line parametrization considers the free parameters to be redshift independent. The redshift-dependence of SFR is through the characteristic time-scale, i.e. $\dot{M}_\star = \frac{M_\star}{t H^{-1}(z)}$, which leads to $\dot{M}_\star \sim (1+z)^{3/2}$ during the matter dominated epoch (see the motivation of this form in Park et al. 2019). While this assumption successfully describes the observed UV LFs, one could consider also a more flexible redshift evolution (e.g. Mirocha et al. 2017; Mirocha 2020).

Thereby, we additionally test a model with $f_\star = f_\star(z)$ in the following form:

$$f_\star = f_{\star,6}(M_\mathrm{h}) \left(\frac{1+z}{7}\right)^\gamma , \tag{A1}$$

where γ is an additional free parameter and $f_{\star,6}(M_\mathrm{h})$ is the star formation efficiency at $z = 6$ with 'PL' or 'DPL' halo mass dependency. We assume a flat prior for γ over the range $(-3/2, 3/2)$.

We calculate Bayes factors for WDM and CDM using this redshift-dependent star formation efficiency, with respect to the fiducial CDM with a redshift-independent $f_\star$. The results are shown in Table A1.

Table A1. Base 10 logarithms of Bayes factor for various DM scenarios and with 'PL' and 'DPL' $f_\star$ halo mass dependency and on the assumption of redshift dependency according equation (A1). The evidences are calculated on the 'B + ' data set. The CDM scenario with 'PL' redshift-independent star formation efficiency is assumed as a fiducial model.

CDM		WDM	
PL	DPL	PL	DPL
-0.48 ± 0.09	-0.18 ± 0.09	-0.56 ± 0.1	-0.73 ± 0.1

We don't find any support for such a redshift-dependent $f_\star$. Moreover, the WDM scenario with a redshift-dependent $f_\star$ is substantially disfavoured. Also, the most probable values of γ are close to 0 for all cases under consideration. We thus conclude that there is currently no need for a redshift evolution in the star formation efficiency, consistent with previous works (Oesch et al. 2018; Park et al. 2019; Bouwens et al. 2021).

APPENDIX B: HALO MASS FUNCTION WITH ALTERNATIVE PARAMETRIZATION

While the sharp k-space filter allows one to capture the low-mass end of WDM HMF reasonably well, the high-mass end is systematically underestimated (e.g. up to 15–20 per cent at $z = 6$ using the Sheth–Tormen form; see more in Schneider, Smith & Reed 2013; Schneider 2015). We have found that the simulations from Schneider (2015) and Bose et al. (2016) are well-described on both high- and low-mass scales by the Sheth–Tormen approximation with the following parameters: $A_{ST} = 0.322$, $q = 0.93$, and $p = 0.3$.

We repeat all of our calculations with these parameters, and do not find any significant difference with results obtained in our base-line model, see Table B1and B2.

Table B1. The obtained 95% lower bounds (in keV) on the WDM particle mass resulting from different data sets and model choices, using alternative halo-mass function parameters.

	WDM, 'PL'	WDM, 'DPL'
A18	1.41	1.40
B17	2.03	2.03
B +	2.08	2.14

Table B2. Base 10 logarithms of the Bayes factor, which is calculated for warm DM scenario with alternative halo-mass function parameters versus cold DM with 'PL' $f_\star$.

	WDM, 'PL'	WDM, 'DPL'
A18	0.13 ± 0.09	0.01 ± 0.09
B +	-0.14 ± 0.09	-0.35 ± 0.1
B17	-0.24 ± 0.09	-0.18 ± 0.09

APPENDIX C: POSTERIOR PROBABILITY DISTRIBUTIONS

The corner plots corresponding to our astrophysical models, PL and DPL, and three data sets ('A18', 'B17', and 'B + ') are shown in Fig. C1 (PL $f_\star$) and Fig. C2 (DPL $f_\star$). The 2D marginalized posterior regions show the degeneracy between the DM free-streaming properties (encoded by the inverted WDM particle mass $1/m_x$) and the characteristic turnover halo mass scale set by baryonic physics, M_t. We confirm that the posteriors calculated via DYNESTY are fully consistent with the MCMC results, which additionally verifies the robustness of the inference.

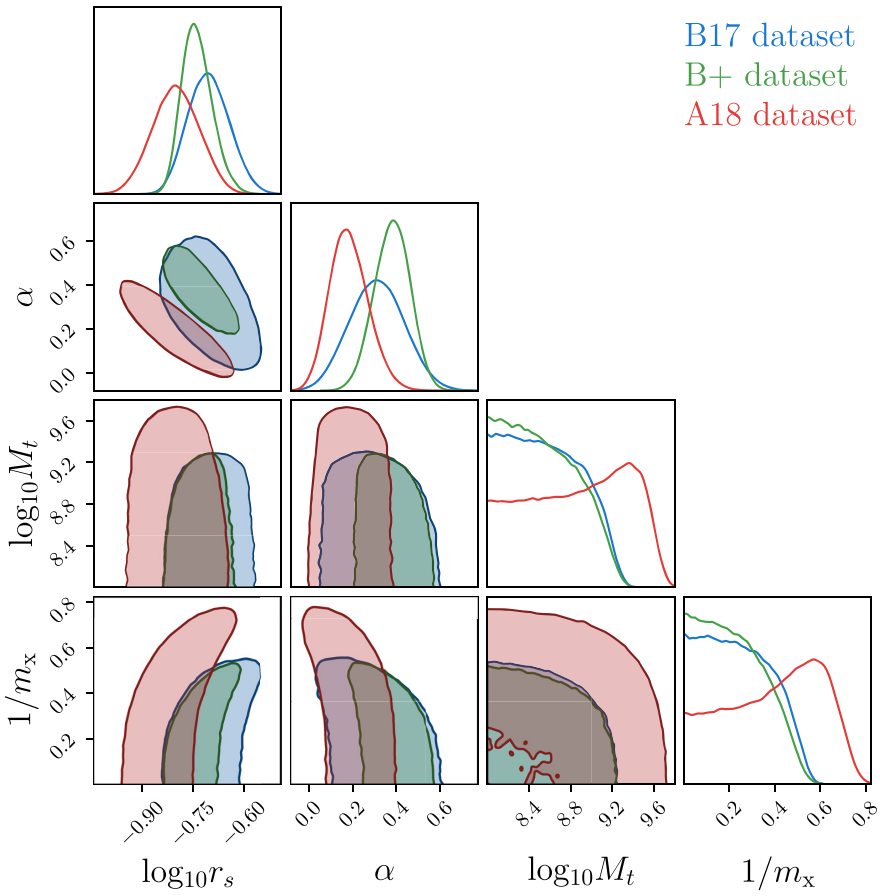

Figure C1. Corner plot showing parameter constraints, obtained from the MCMC analysis of A18, B17, and B + data sets with the simple power-law star formation efficiency model (PL): the 95 per cent contours of the joint 2D marginalized posterior distributions with PDF along the diagonal.

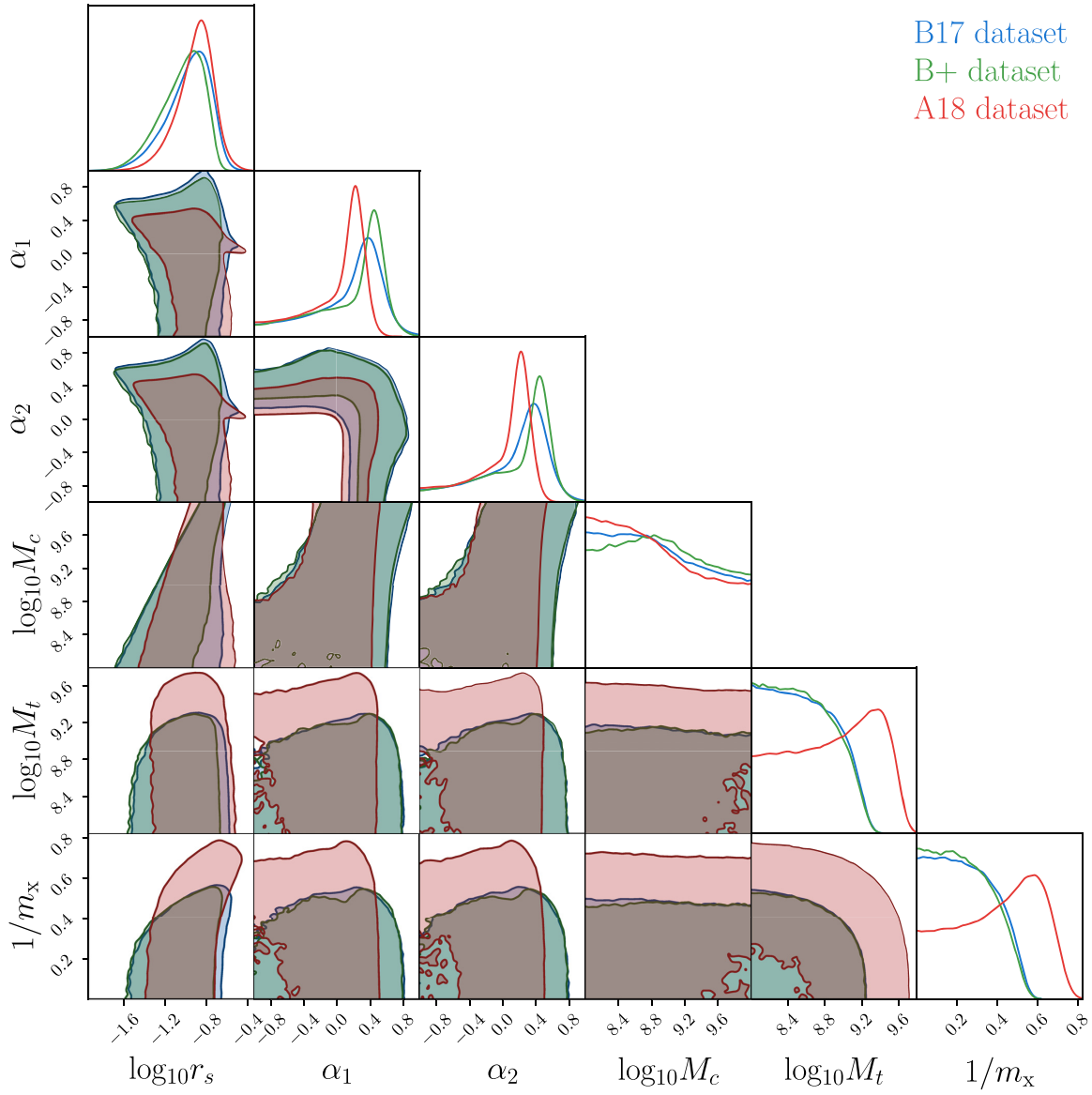

Figure C2. The same as in Fig. C1, but in the case of DPL model.

This paper has been typeset from a TEX/LATEX file prepared by the author.